ACS APPLIED MATERIALS & INTERFACES

www.acsami.org

Research Article

Proton-Assisted Redox-Based Three-Terminal Memristor for Synaptic Device Applications

Lingli Liu, Putu Andhita Dananjaya, Mun Yin Chee, Gerard Joseph Lim, Calvin Xiu Xian Lee, and Wen Siang Lew*

Cite This: *ACS Appl. Mater. Interfaces* 2023, 15, 29287−29296

Read Online

ACCESS | Metrics & More | Article Recommendations | Supporting Information

ABSTRACT: Emerging technologies, i.e., spintronics, 2D materials, and memristive devices, have been widely investigated as the building block of neuromorphic computing systems. Three-terminal memristor (3TM) is specifically designed to mitigate the challenges encountered by its two-terminal counterpart as it can concurrently execute signal transmission and memory operations. In this work, we present a complementary metal-oxide-semiconductor-compatible 3TM with highly linear weight update characteristics and a dynamic range of ∼15. The switching mechanism is governed by the migration of oxygen ions and protons in and out of the channel under an external gate electric field. The involvement of the protonic defects in the electrochemical reactions is proposed based on the bipolar pulse trains required to initiate the oxidation process and the device electrical characteristics under different humidity levels. For the synaptic operation, an excellent endurance performance with over 256k synaptic weight updates was demonstrated while maintaining a stable dynamic range. Additionally, the synaptic performance of the 3TM is simulated and implemented into a four-layer neural network (NN) model, achieving an accuracy of ∼92% in MNIST handwritten digit recognition. With such desirable conductance modulation characteristics, our proposed 3T-memristor is a promising synaptic device candidate to realize the hardware implementation of the artificial NN.

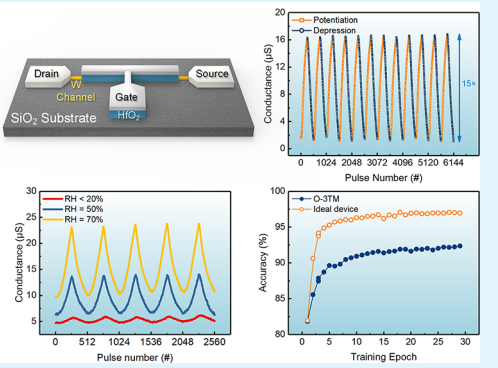

KEYWORDS: *neuromorphic computing, three-terminal, memristor, synaptic device, humidity*

INTRODUCTION

The complementary metal-oxide-semiconductor (CMOS) technology has been progressively advancing to fulfill the ever-growing demands in computing. The current computational paradigm is based on the conventional von Neumann architecture, dependent on progress in CMOS transistor performance improvement and scaling, in alignment with Moore's law and Dennard's scaling observations.[1] The von Neumann architecture is designed with separate regions allocated for processing and memory interconnected by data buses. While technological demands have been fulfilled by such an architecture, the growing performance discrepancy between processing and memory units sees an impending limit imposed by performance and scalability.[2] Neuromorphic computing architecture, capable of parallel data processing, can overcome the von Neumann bottleneck.[3,4] Furthermore, the biological brain inspires in-memory computing for greater time and energy efficiency.[5] Extensive studies have been made on the hardware implementation of artificial neural networks (NNs), comprising the fundamental building blocks: artificial neurons and synapses.[6,7]

In the biological brain, the connection strength between neurons is regulated by a synaptic weight. In an artificial synaptic device, analog-resistive switching behavior is used to mimic the modulation of the synaptic plasticity.[8,9] Various memristive devices enable analog switching, such as ferroelectric random-access memory,[10,11] phase-change random-access memory,[12] and resistive random-access memory (RRAM).[13] These two-terminal (2T) memory technologies have been thoroughly investigated as artificial synapses in prototype NNs.[14−17] However, 2T synaptic devices face a challenge in simultaneously performing signal transmission and learning function due to the shared writing/reading path.[18] The shared writing and reading paths would induce extensive noise and disturbance, resulting in reliability issues.[19] Additionally, 2T memristors normally exhibit a nonlinear conductance change under identical programming pulses, which is not ideal especially for in situ learning applications. A linear conductance modulation (i.e., linear weight updating behavior) enables the direct mapping of the weights in the algorithms to the device conductance states, which leads to

Received: March 20, 2023
Accepted: May 22, 2023
Published: June 12, 2023

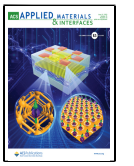

Downloaded via NANYANG TECHNOLOGICAL UNIV on June 28, 2023 at 06:44:29 (UTC).
See https://pubs.acs.org/sharingguidelines for options on how to legitimately share published articles.

ACS Publications

© 2023 American Chemical Society

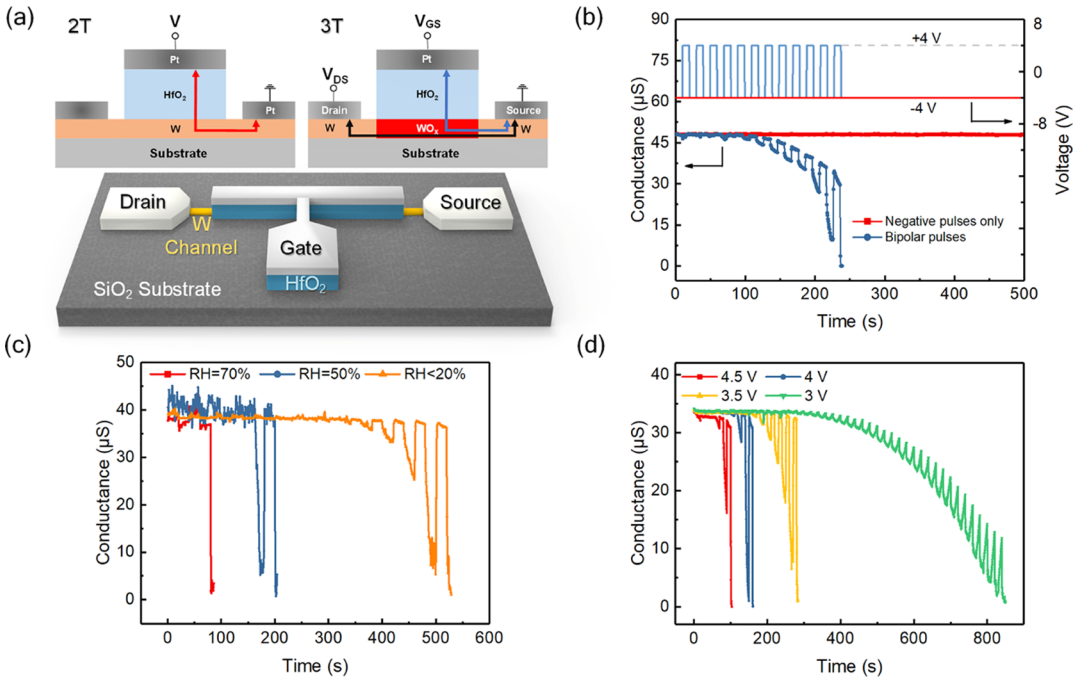

Figure 1. (a) Schematic and two operation modes of the proposed memristor. (b) Conductance changes during the forming process under bipolar (±4 V, 0.5 s) and negative (−4 V, 0.5 s) gate pulses. Only under the bipolar pulses, the W channel would be electrochemically oxidized. (c) Forming process under different RH values, a higher RH leads to a faster forming process. (d) Forming process under fixed negative pulses (−4 V, 0.5 s) and varied positive pulse amplitudes (3/3.5/4/4.5 V, 0.5 s). Positive pulses with higher amplitude enable the protons to reach the surface faster, causing faster oxidation.

higher training accuracy.[20] To overcome these challenges, an additional gate terminal is introduced to decouple the writing/reading paths and enable more predictable analog conductance update behavior.[5,21]

A 3T memristor (3TM) can achieve analog conductance modulation when active ions [e.g., H^+ (proton), Li^+, or O^{2-}] are doped/de-doped from the electrolyte into the channel.[22−24] The ion concentration in the channel can be tuned by applying voltage pulses on the gate, while the change in the channel conductance is read out through the drain and source terminal.[25] Due to the high reactivity of light cations and the challenges they pose on the large-scale integration, investigations on more CMOS compatible oxygen ion based-3TM (O-3TM) have been an emerging topic of interest.[9,24,26] Recently, O-3TM consisting of TiO_{2-x} and WO_3 switching layers with YSZ electrolytes have demonstrated superior stability with highly linear conductance modulation.[5,27] In general, the fabrication process of all reported O-3TM devices involves water or other solvents (e.g., lithography, lift-off, etc.) containing moisture/protons.[5,27,28] Furthermore, the moisture in the test environment can penetrate the device capping layers or side walls, acting as a proton source. Thus, the inherent presence of protons in the device structure becomes inevitable owing to the background moisture during the fabrication process and the device operation even if the device is encapsulated.[29] However, such impact of humidity on the redox switching of O-3TMs is rarely investigated.

Protons from the moisture in air act as n-type dopants in some oxides channel (e.g., VO_2 and WO_x), more protons in the channel lead to a higher channel conductivity.[23,30] Meanwhile, the oxides channel deficient/rich in O^{2-} can also be co-related to high/low conductivity.[27] In this work, we developed a CMOS-compatible O-3TM consisting of a Pt layer (gate electrode), a HfO_2 layer (electrolyte), and a W layer (channel). To avoid the impact of gate leakage, the high-κ dielectric HfO_2 with an excellent time-dependent dielectric breakdown performance and good oxygen mobility is considered.[24,31−33] These materials allowed the implementation of standard established CMOS-fabrication techniques, paving the way for future integration with CMOS circuitry.

The proposed working mechanism of our O-3TM is driven by the migration of protons and O^{2-} from the channel to the electrolyte or vice-versa under the external gate electric field. It is based on the bipolar pulse trains required to initiate the switching operation (oxidation of the W channel) and the device electrical response under different levels of humidity. The humidity influences the rate of the electrochemical oxidation process of the channel, which is experimentally observed under electrical tests. Such O-3TM demonstrated highly linear channel conductance change behavior, together with stable endurance performance, and high accuracy on pattern recognition simulation based on MNIST data set. All these results suggest that this device has the potential to function as a reliable synaptic element in neuromorphic systems.

RESULTS AND DISCUSSION

The device comprises an HfO_2 insulating layer sandwiched between W and Pt as the channel and the inert electrode, respectively. Depending on the choice of reading and writing paths, the device can be configured into 2T and 3T operating modes, as shown in Figure 1a. In the 2T configuration, the shared writing/reading path is indicated by the red arrow. Typical IV characteristics of the 2T Pt/HfO_2/W device under direct current (DC) voltage sweep are presented in Figure S1. The forming voltage required to initiate the switching is

https://doi.org/10.1021/acsami.3c03974
ACS Appl. Mater. Interfaces 2023, 15, 29287−29296

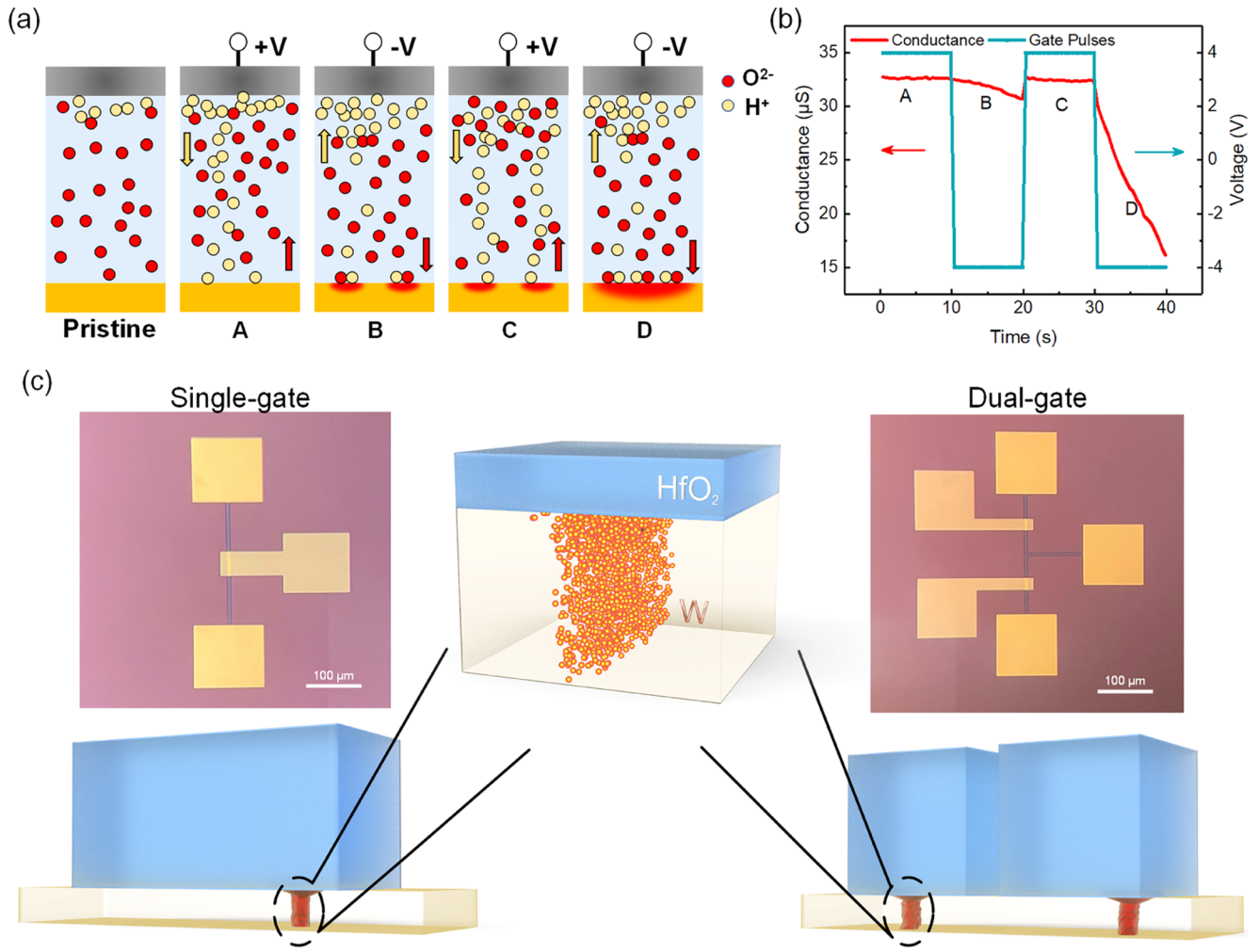

Figure 2. (a) Gradual activation of the proton transportation in the HfO_2 layer under bipolar pulse scheme. Yellow and red arrows indicate the migration direction of protons and O^{2-}, respectively. With positive pulses, the protons move toward the W while O^{2-} move oppositely. Under negative pulses, the migration direction of proton and O^{2-} is reversed. Once the protons reach the W surface, the electrochemical oxidation happens with the conductance change indicated in (b) with respective pulse polarities. (c) Structures of the single- and dual-gate devices and the schematic of localized oxidation of the W. This initial oxidation does not occur across the entire HfO_2/W surface. The red area represents the oxidized W regions.

expected to be high (~7.0 V) due to the relatively thick HfO_2 layer. This forming process induces localized oxygen vacancy defect formation within the RRAM structure. In the process, the compliance current of 100 μA was implemented to prevent the permanent breakdown of the device upon forming from excessive defect generation. The subsequent SET and RESET operations were observed at ~1.3 and −2.7 V, respectively. These IV characteristics are typically observed in filamentary-type of RRAM devices.[34,35]

Under the 3T operating mode, the writing (blue arrow) and reading (black arrow) paths are decoupled. To initiate the switching operation of the O-3TM, a forming process is required to induce W channel oxidation under an external electric field. Several studies have reported that such a forming step can be achieved by applying a train of negative pulses to the gate, inducing O^{2-} ion migration toward the channel, resulting in channel oxidation at the interface. This channel oxidation is indicated by the decreasing channel conductance.[21,36,37] For the developed O-3TM device in this work, the train of negative pulses (−4 V, 0.5 s) failed to oxidize the channel, indicated by the absence of change in channel conductance (Figure 1b, red). It was found that a bipolar pulse scheme (±4 V, 0.5 s) comprising alternating pulse polarities on the gate was required to induce the electrochemical oxidation process (Figure 1b, blue). Pulse trains applied in this work have the same 1 μs rise/fall time, the pulse interval is varied according to the pulse duration, and the off time between pulses is fixed as 400 ns. The pulse information is given in the form of (pulse amplitude and pulse duration). With consecutive positive pulses, the drop in conductance due to negative pulses becomes larger. This forming process was also found to be dependent on the ambient humidity, as presented in Figure 1c. With the bipolar pulse scheme, the forming process is enhanced as the humidity increases. When pristine devices were placed under relative humidity (RH) of <20%, the oxidation of W took approximately six times longer than that of a higher humidity condition (RH ~ 70%).

It has been reported that the presence of moisture absorbed by the porous oxide layers is essential for the redox reaction in RRAM devices.[29,38] For our device, the water molecules would first be chemically absorbed on the surface and the grain

https://doi.org/10.1021/acsami.3c03974
ACS Appl. Mater. Interfaces 2023, 15, 29287−29296

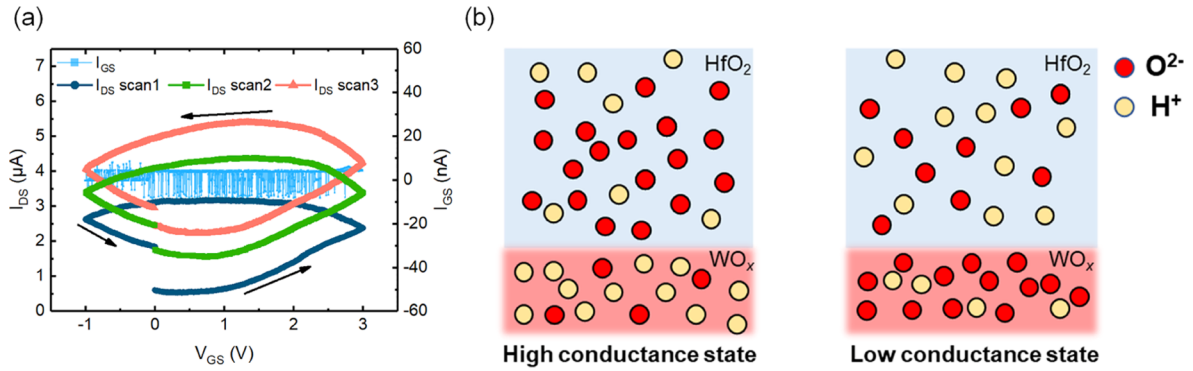

Figure 3. (a) $I-V$ characteristics of the 3T mode. These three hysteresis loops represent the change of I_{DS} with the applied V_{GS}. Gate current I_{GS} in the nA range shows a negligible gate leakage current. The arrows indicate the loop direction. (b) Schematic of the channel under high and low conductance states with different amounts of protons and O^{2-} inside.

boundaries of HfO_2, interacting with the oxygen vacancies through the following process

$$H_2O + O_o^x + V_o^{\bullet\bullet} \leftrightharpoons 2OH_o^{\bullet}$$

in which the $OH_o^{\bullet}$ represents a proton being bonded to an oxygen ion of the metal oxide.[39−41] The protons from the subsequent physically absorbed water can hop through the $OH_o^{\bullet}$ network, resulting in protonic conduction governed by the Grotthuss mechanism within the HfO_2 layer.[39,42] As shown in Figure 2a, when the positive pulses arrive, the protons are pumped toward the HfO_2/W interface while the O^{2-} in the HfO_2 would move in the opposite direction. The hydroxyl groups inside HfO_2 allow the protons to travel and ionize the W surface (A,C). When negative pulses are applied, the O^{2-} driven to the W surface starts to oxidize the ionized W (B,D) with the assistance of the electron acceptor, i.e., proton. Figure 2b indicates the conductance change under positive and negative pulses. With higher humidity, more hydroxyl groups would be formed, and more protons would reach the W surface, resulting in a faster oxidation process.[43] Supplementary measurements were conducted with fixed negative pulses (−4 V, 0.5 s) but different positive pulses (3/3.5/4/4.5 V, 0.5 s), in which a higher positive pulse enables the protons to reach the W surface faster, leading to a faster oxidation process, as shown in Figure 1d. To confirm that the source of O^{2-} is the HfO_2, XPS depth profiling was performed on a pristine device and the devices under 2T and 3T modes after forming operation. The XPS spectra of Hf, O, and W are shown in Figures S2−S5. The spectra can be divided into bulk HfO_2 (<60 s), HfO_2−W interface (60−70 s), and bulk W region (>70 s). The Hf spectra in Figure S2 indicate the presence of different hafnium suboxide states in each device. In the pristine device, HfO_2 and HfO_{2-x} oxide can be found in the bulk region, while the HfO suboxide is found at the HfO_2−W interface. Meanwhile, the 2T device shows an additional metallic Hf in the bulk and interface region, suggesting the presence of localized conductive paths within the dielectric. In the 3T device, suboxides (HfO, HfO_{2-x}, and HfO_2) are present in the bulk and interface, without the metallic Hf. Unlike the soft broken-down of the HfO_2 in the 2T device, HfO_2 in the 3T device remains insulating. This suggests that O^{2-} are provided by HfO_2, and the W channel is effectively oxidized, which can be further confirmed by the W spectra. Additionally, the existence of the metal-hydroxyl interaction and H_2O in the O 1s spectra of the 3T device indicates the humidity-promoted oxygen migration. Unless specifically stated, all the following tests were performed under ambient humidity of RH ∼ 50%.

Another experiment was designed to verify whether this oxidation occurs at the entire channel−oxide interface or in localized regions. Single-gate and dual-gate devices were fabricated with identical device areas (the gate width for the single-gate device is twice that of the dual-gate one), as shown in Figure 2c. The two devices in the dual-gated configuration were formed independently under the same condition as the single-gated devices. After the forming process, it was found that the dual-gate device always has a more insulating channel, indicating non-area-dependent oxidation. The channel resistances for these two devices are present in Table S1. Thus, a localized oxidation model is proposed, as depicted in Figure 2c, in which the red area represents the oxidized W. This localized oxidation promises the scalability potential of the device, which is suitable for high-density synaptic array implementation. To prove its scalability, devices with various channel lengths and widths were fabricated, seeing Figure S6a. The channel length (the area under the HfO_2 layer) was varied from 40 to 5 μm, and the channel width was varied from 5 to 0.5 μm. The forming process of each device was successfully performed, in which the forming time for all devices is around 100 s (Figure S6b−e). There is no obvious trend for the forming time with the change of the channel dimensions. After the forming process, all devices successfully performed repeatable P/D behaviors, indicating the scalability of the device.

The W channel of each O-3TM was oxidized from ∼40 to ∼20 nS. DC sweeps on the channel before and after the oxidation was performed, and a transition of the $I-V$ characteristics from linear to nonlinear was observed, as shown in Figure S7a. To further verify the current conduction mechanism of the channel, the nonlinear $I-V$ curve was plotted in the log−log scale and linear fitted (Figure S7b). The slope value of the current increases with the voltage, from 0.997 to 2.654, suggesting a charge-limited current conduction mechanism.[44] By fixing the drain reading voltage (V_{DS}) as 0.2 V and dual sweeping the gate voltage (V_{GS}) between −1 and 3 V, the change of channel current (I_{DS}) and gate current (I_{GS}) is shown in Figure 3a. Ionic switching behavior with a large counterclockwise hysteresis loop is observed in the O-3TM. Compared with the channel current (in the μA range), the gate leakage current (in the nA range) is negligible, indicating notable insulating properties of the HfO_2 electrolyte. The fluctuation of I_{GS} is due to measurement limitations. Similar to the initial oxidation process, the electric field (E_{ext}) generated

https://doi.org/10.1021/acsami.3c03974
ACS Appl. Mater. Interfaces 2023, 15, 29287−29296

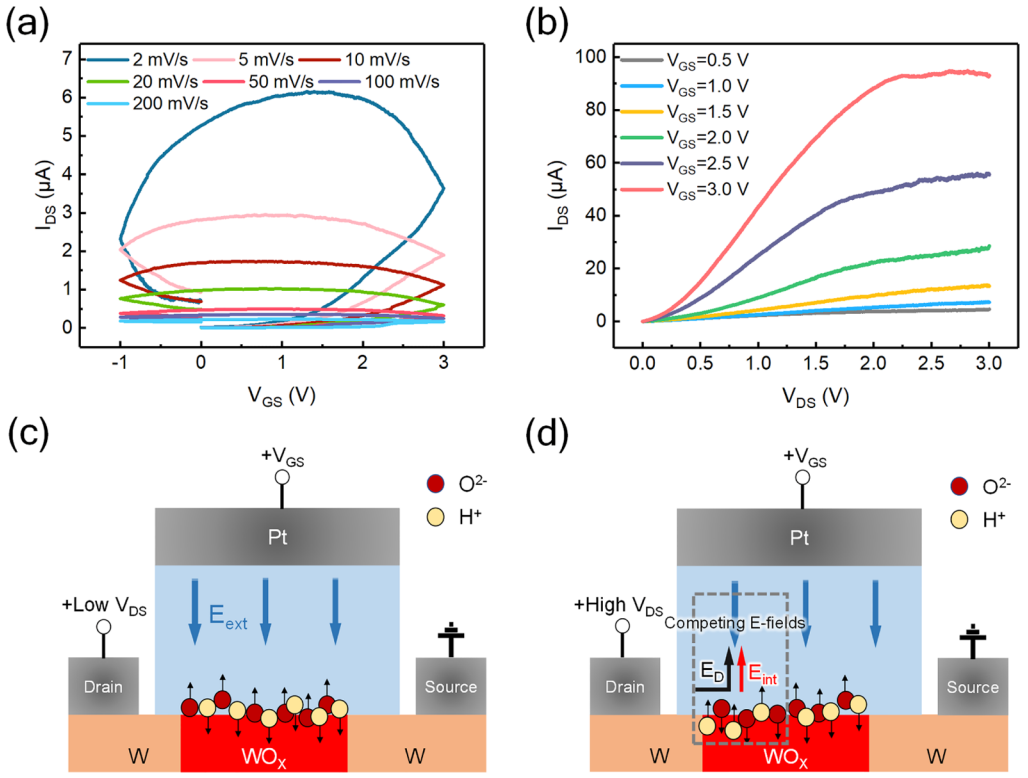

Figure 4. Transfer and output characteristics of the O-3TM device. (a) Transfer characteristics under different scan rates of the V_{GS}. (b) Output characteristics under different amplitude of V_{GS}. (c) Mobile ion migration in the linear region. (d) Mobile ion migration in the saturation region.

by the gate pulse would drive the negatively charged O^{2-} and positively charged proton in the opposite direction, causing the channel conductance to change. Under positive pulses, the WO_x channel is rich in proton but deficient in O^{2-}, showing a high conductance state. In contrast, more O^{2-} and less proton in the channel with negative pulses applied would result in a low conductance state. Figure 3b shows the schematic of the O-3TM when the channel is in a high conductance state and a low conductance state. DC sweep of the channel under low and high conductance states is shown in Figure S7c, and the more linear $I-V$ curve of the high conductance state indicates that part of the WO_x channel was reduced back to W by the positive pulses.

The gate-controlled configuration of the O-3TM is very similar to a transistor, with the semiconductor channel replaced by the WO_x layer. With the transfer and output characteristics given in Figure 4, an n-type enhancement-mode transistor-like performance can be observed in the O-3TM.[45] Figure 4a shows the transfer curves under different scan rates of V_{GS}. A slower scan rate correlates to a bigger hysteresis loop and a larger high/low current ratio when V_{GS} = 0 V. With a faster scan rate, a smaller amount of mobile ions would be migrated, resulting in a smaller current change. In comparison, a slower scan rate allows more mobile ions to be activated and migrated, contributing to a more pronounced current change. The output characteristics were obtained by sweeping the V_{DS} from 0 to 3 V at different V_{GS}, as shown in Figure 4b. Like a MOSFET, the device also exhibits linear and saturation regions. For a MOSFET, the saturation region appears when the inversion layer starts to pinch off due to the high drain voltage. Nevertheless, the saturation region for the O-3TM can be assigned to the competition between different electric fields. With positive V_{GS} applied, the E_{ext} pumps the mobile ions to migrate accordingly until the channel is depleted of O^{2-} and rich in the proton. At the same time, the concentration gradient of O^{2-} and proton would generate an increasing internal electric field (E_{int}) that has the opposite direction to the E_{ext}. The applied V_{DS} also introduces an electric field (E_D) near the drain terminal. In the linear region, the E_{ext} overwhelms E_{int} and E_D and leads to a monotonic rise in conductance (Figure 4c). With the increase of E_D and the strong E_{int} introduced by high V_{GS}, the E_{ext} cannot keep modulating the ion concentration of the channel, leading to the saturation region (Figure 4d).

With the O^{2-}/proton migration in and out of the WO_x channel, this O-3TM can be operated as an artificial synapse.[9,27] The synaptic weight is represented by the channel conductance, which can be tuned by the applied gate pulses, thus emulating the weight updating in biological synapses. The increase or decrease of synaptic weight is called potentiation (P) and depression (D). For artificial synapses, a linear, symmetrical, and multi-bit P/D behavior with a large dynamic range is critical for the training accuracy of a NN.[12,27] A model is used to evaluate the nonlinearity of the P/D process (see eqs S1−S3).[45,46] For the ideal P/D curve, the nonlinearity factor "A" value is 0.

For the developed O-3TM device, the synaptic operations, i.e., potentiation and depression, are performed by applying positive and negative voltage pulses on the gate, respectively. Figure S8a shows the P/D curves with 20 potentiation pulses (2.8 V, 50 ms) followed by 20 depression pulses (−0.8 V, 50 ms) under a fixed read V_{DS} of 0.2 V. The potentiation curve achieved a nonlinearity factor of 2.40, while significantly less linear depression behavior with a nonlinearity factor of 7.16 was obtained. The linearity of the depression curve is improved as the negative voltage amplitude of the depression is reduced,

https://doi.org/10.1021/acsami.3c03974
ACS Appl. Mater. Interfaces 2023, 15, 29287−29296

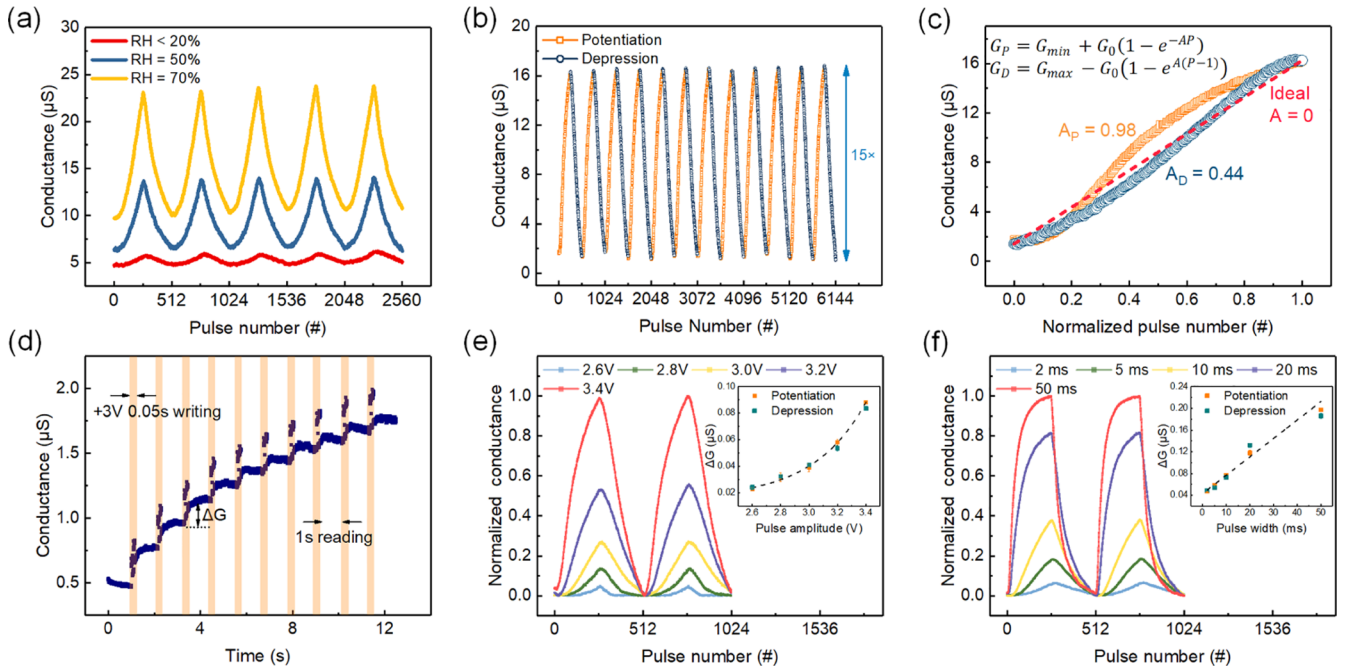

Figure 5. Measured channel conductance modulation of O-3TM by applying gate pulses. (a) P/D curves under different RH. Under a higher humidity condition, the conductance window becomes wider, in addition to a higher minimum conductance state. (b) P/D curves of the O-3TM were obtained by applying 256 P/D programming pulses with an amplitude of 3/0 V and a duration of 5 ms. The V_{DS} is fixed as 0.2 V to read out the channel conductance. (c) Nonlinearity analysis of the P/D curves with A_P of 0.98 and A_D of 0.44 indicates quasi-linear and symmetry weight update behavior. (d) Conductance changes after each writing pulse (3 V, 50 ms, space 1 s). Reading time of 1 s with no voltage applied to monitor the conductance states between two pulses. (e) Potentiation pulse−amplitude-dependent P/D curves of the O-3TM. Pulse duration is fixed as 5 ms. ΔG is exponentially dependent on the pulse width (inset). (f) Potentiation pulses-width-dependent P/D curves of the O-3TM. P/D pulse amplitude is fixed as 3/0 V. ΔG increases linearly with the pulse width (inset).

as depicted in Figure S8a−d. The smallest nonlinearity factor was achieved under 0 V in which no external gate pulses were applied, and the conductance state was read every 50 ms to match the potentiation duration. This voltage-dependent depression performance indicates that the ideal depression behavior is governed by the self-diffusion of the O^{2-}/proton mechanism rather than applying an external electric field to drive them.

First, the P/D behavior under different humidity was investigated by sequentially programming the O-3TM with 256 potentiation pulses (2.8 V, 5 ms) followed by 256 depression pulses (0 V, 5 ms) and fixing the V_{DS} as 0.2 V. The device presents a wider conductance window and a higher minimum conductance state with the increase of humidity, as shown in Figure 5a. As more protons migrate toward the channel and participate as charge carriers in a more humid condition, a more pronounced conductance change could be observed. Under opposite pulse polarities, the channel conductance increases or decreases due to the movement of protons and O^{2-}. However, to simplify the description of the ion migration, we will only focus on the migration of O^{2-} in the subsequent discussion.

When writing the device with 256 3/0 V (5 ms) pulses, the device features good linearity of P/D with a large conductance dynamic range of ∼15 under ambient humidity (Figure 5b). As Figure 5c shows, the nonlinearity factor of potentiation (A_P) and depression (A_D) is 0.98 and 0.44, respectively, indicating a quasi-linear conductance update behavior. In contrast, the P/D curves of the device under 2T operation mode are nonlinear and unpredictable (A_P = 10.68, A_D = 13.43, Figure S9). Figure 5d reveals the conductance change (ΔG) after each writing pulse (3 V, 50 ms). In between each pulse, the conductance was monitored for 1 s. As shown in Figure 5d, for higher conductance states, more O^{2-} are extracted out of the channel, which correlates to a higher E_{int}, so the diffusion of O^{2-} back into the channel will be enhanced after the removal of E_{ext}. A small positive voltage of 0.8 V can be applied to hold each conductance state, and the retention of 1000 s for 10 chosen conductance states is shown in Figure S10.

For the O-3TM, the applied gate pulses with different amplitude or width would extract the O^{2-} to varying degrees, thus leading to different P/D behaviors. It is necessary to inspect the P/D behaviors under different pulse conditions to further investigate the O-3TM programmability. Potentiation pulse-amplitude-dependent and pulses-width-dependent P/D curves are shown in Figure 5e,f, in which the conductance value of each curve is normalized to show a more intuitive trend. In Figure 5e, P/D curves show an increased dynamic range when the potentiation pulse amplitude increases from 2.6 to 3.4 V (pulse duration was fixed as 5 ms), in which the inset indicates that ΔG is exponentially dependent on the pulse amplitude. Figure 5f shows the P/D curves with the potentiation pulse-width varying from 2 to 50 ms under fixed pulse amplitude as 3 V. The dynamic range increases with the pulse width while the linearity degrades instead. When the pulse width is 20 ms and above, the conductance increases or decreases rapidly at first but becomes saturated at the end of the process. The inset in Figure 5f shows that the ΔG has an approximately linear relationship with the pulse width. It still offers a distinctive ΔG of 47 nS when the pulse width is decreased to 2 ms, demonstrating a high-speed switching compared with reported oxygen-ion based synaptic devices.[27]

https://doi.org/10.1021/acsami.3c03974
ACS Appl. Mater. Interfaces 2023, 15, 29287−29296

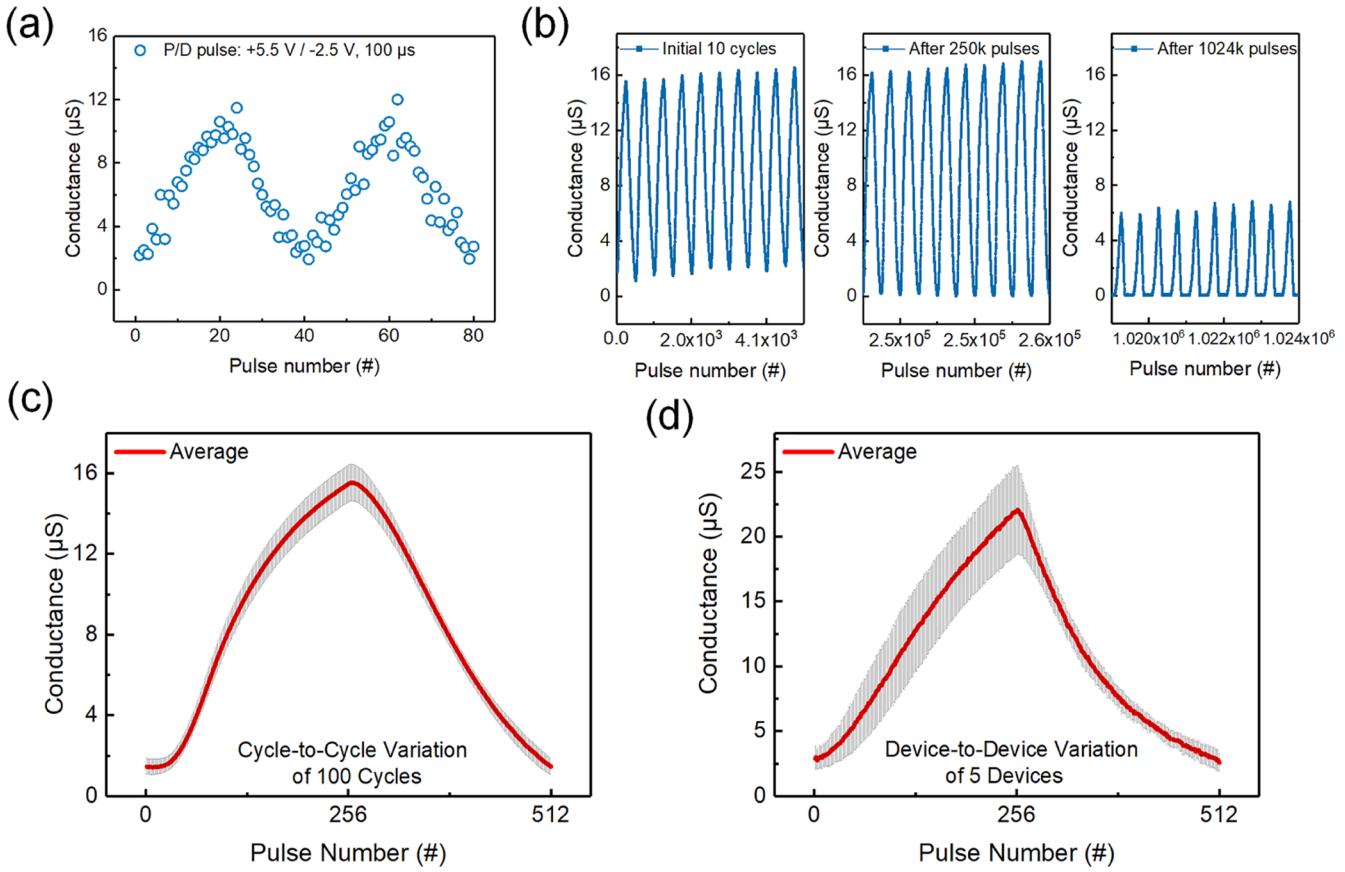

Figure 6. (a) Fast-switching speed of 100 μs is demonstrated in the O-3TM. (b) Excellent endurance performance of over 256k pulses, P/D pulses were fixed as 3/0 V, 5 ms. (c) Cycle-to-cycle and (d) device-to-device variation of the O-3TM, in which the red line indicates the average value, and the gray error bars are the respective standard deviation.

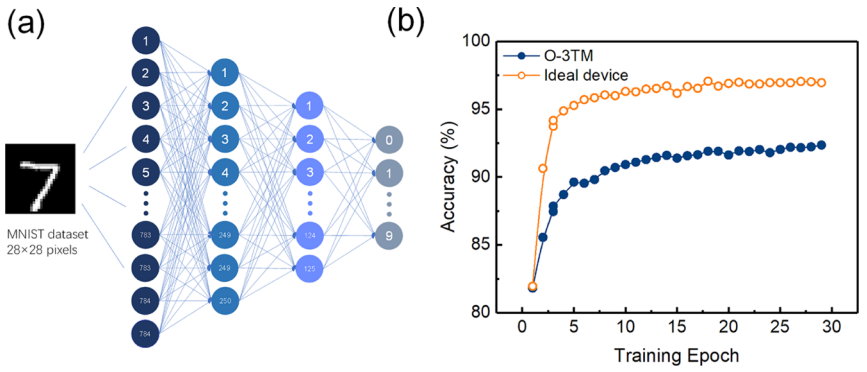

Figure 7. (a) Schematic of the four-layer neuron network for the pattern recognition simulation architecture. Each node represents the neuron, and each connection represents the synapse. (b) Pattern recognition accuracies based on the ideal synaptic device and the O-3TM.

The switching speed of synaptic devices is a vital characteristic for online training of NN s, which is determined by the duration of the programming pulse.[47]

To further investigate the speed limit of the O-3TM, it is programmed with 20 potentiation pulses and 20 depression pulses with higher amplitude and shorter pulse width. Conductance modulation of the O-3TM is demonstrated with a pulse width of 100 μs (Figure 6a), indicating that a fast-switching speed is possible in the O-3TM. For online training, the weights of each synapse are updated frequently, which puts forward requirements on the endurance performance of synapses.[20] Strong endurance characteristics are demonstrated in Figure 6b by repeatedly programming the device with 256k pulses. More than 500 stable P/D cycles can be achieved with 256 conductance updates for each P/D process. As the device underwent more P/D cycles, the conductance started to decrease and eventually stuck in the lower conductance state (a significant drop can be observed after 2000 P/D cycles). This is potentially due to the expansion of the oxidized W region during device operation, which leads to fully oxidized W channel. Except for the speed and endurance requirements, small device-to-device and cycle-to-cycle variations are also crucial for high training accuracy.[48] Figure 6c shows the cycle-to-cycle variation of 100 cycles. A steady operation without significant degradation of the P/D performance is observed with an average variation of 3.6%. Besides, the device-to-device

https://doi.org/10.1021/acsami.3c03974
ACS Appl. Mater. Interfaces 2023, 15, 29287−29296

variation was obtained from five devices with an average variation of 18.9%, as shown in Figure 6d. The variation for the potentiation is a bit higher than that of the depression process, which can be attributed to the different oxidation degrees of the W channel during the initial oxidation process. Such a low variation could empower the O-3TM to implement the NN as the synapse with higher stability. Error bars in Figure 6 represent the standard deviation of the conductance update, and the variation is calculated by dividing the standard variation by the averaged conductance value.

In order to evaluate the performance of the O-3TM as an artificial synapse, a pattern recognition simulation was conducted within a four-layer NN. The NN consists of one input layer (784 neurons), two hidden layers (250 and 125 neurons), and one output layer (10 neurons), in which every two neurons are connected by synapses (Figure 7a).[49] Patterns for the recognition training are handwritten digits (0 to 9) from the Modified National Institute of Standards and Technology (MNIST) database with 28 × 28 pixels. For each epoch, 50,000 images from the MNIST training set and 10,000 images from the MNIST test set are used for training and testing, respectively.[50] During the training process, the weight of each synapse is being updated according to the linearity, dynamic range, and precision extracted from Figure 5b. After 30 training epochs, the high recognition accuracy of 92.36% can be achieved by the O-3TM (Figure 7b). The same simulation was conducted using an ideal synaptic device with perfect linearity ($A_P = A_D = 0$), infinite dynamic range, and infinite conductance states, achieving 97.07% accuracy. Compared with the ideal case, the O-3TM is an up-and-coming candidate as the artificial synapse for neuromorphic computing.

CONCLUSIONS

In summary, a CMOS compatible O-3TM based on O^{2-}/proton migration has been developed as an artificial synapse. It shows nearly linear potentiation ($A_P = 0.98$) and depression ($A_D = 0.44$) behavior under identical pulses operation, while maintaining a stable dynamic range of ∼15. The initial electrochemical oxidation process is found to be dependent on the humidity level. The higher oxidation rate is observed under higher humidity because of the proton-assisted mechanism. In addition, the electrochemical oxidation of the W during the forming process is not area dependent, thus providing the scalability potential on the device level. A relatively fast switching speed of 100 μs and high endurance of more than 256k weight updates were also demonstrated in this O-3TM. The high MNIST pattern recognition accuracy of 92.36% achieved by the O-3TM indicates its capability to act as an artificial synapse in the next generation of the neuromorphic system.

EXPERIMENTAL METHODS

The O-3TM device was fabricated on a Si ⟨100⟩ substrate with 300 nm thermal oxide above. Before the deposition of each layer, a UV lithography process was conducted to form the desired pattern. Each lithography process started with the spin coating of AZ 5214E photoresist, followed by the soft baking for 90 s at 115 °C and exposure under the SUSS Microtec MJB4 mask aligner for 13 s with the patterned mask. First, the 5 nm thick W channel layer was deposited by DC sputtering under power conditions of 50 W. Second, a 30 nm thick HfO_2 layer was deposited by radio frequency (RF) sputtering, followed by the 15 nm Pt top electrode deposition by DC sputtering, both under power conditions of 50 W. Lastly, a 20 nm thick Pt was deposited as source/drain contact pads with the size of 150 × 150 μm^2. All sputtering processes were kept at 2 mTorr under Ar ambient at room temperature using the AJA International ATC-Orion 8-target UHV magnetron sputtering deposition system. By using the Keithley 4200A SCS parameter analyzer, the electrical properties and synaptic behaviors of the device were measured in an ambient environment at room temperature.

ASSOCIATED CONTENT

Supporting Information

The Supporting Information is available free of charge at https://pubs.acs.org/doi/10.1021/acsami.3c03974.

Bipolar $I-V$ characteristics of the 2T Pt/HfO_2/W devices; channel resistance for single- and dual-gate device after the oxidation; XPS spectra of Hf 4f for pristine, 2T, and 3T devices under different etching cycles; XPS spectra of O 1s for pristine, 2T, and 3T devices under different etching cycles; XPS spectra of W 4f for pristine, 2T, and 3T devices under different etching cycles; etching time-atomic concentration profiles for W, Hf, and O elements in pristine, 2T, and 3T devices; images of devices with varied channel lengths and widths and respective forming processes; DC sweep of the channel and conduction mechanism fitting; P/D curves under fixed varies depression voltage; P/D curves of the device under 2T operation mode; 10 conductance states retention under 0.8 V holding voltage; and nonlinearity analysis model (PDF)

AUTHOR INFORMATION

Corresponding Author

Wen Siang Lew − *School of Physical and Mathematical Sciences, Nanyang Technological University, Singapore 637371, Singapore;* orcid.org/0000-0002-5161-741X; Email: wensiang@ntu.edu.sg

Authors

Lingli Liu − *School of Physical and Mathematical Sciences, Nanyang Technological University, Singapore 637371, Singapore;* orcid.org/0000-0002-4360-2699

Putu Andhita Dananjaya − *School of Physical and Mathematical Sciences, Nanyang Technological University, Singapore 637371, Singapore;* orcid.org/0000-0001-9416-6455

Mun Yin Chee − *School of Physical and Mathematical Sciences, Nanyang Technological University, Singapore 637371, Singapore;* orcid.org/0000-0002-1580-1463

Gerard Joseph Lim − *School of Physical and Mathematical Sciences, Nanyang Technological University, Singapore 637371, Singapore;* orcid.org/0000-0003-2411-5841

Calvin Xiu Xian Lee − *School of Physical and Mathematical Sciences, Nanyang Technological University, Singapore 637371, Singapore;* orcid.org/0000-0002-5426-2482

Complete contact information is available at: https://pubs.acs.org/10.1021/acsami.3c03974

Notes

The authors declare no competing financial interest.

ACKNOWLEDGMENTS

This work was supported by a RIE2020 ASTAR AME IAF-ICP grant (no. I1801E0030).

REFERENCES

(1) Johnsson, L.; Netzer, G. The Impact of Moore's Law and Loss of Dennard Scaling: Are DSP SoCs an Energy Efficient Alternative to X86 SoCs? *J. Phys.: Conf. Ser.* **2016**, *762*, 012022.

(2) Nawrocki, W. Physical Limits for Scaling of Integrated Circuits. *J. Phys.: Conf. Ser.* **2010**, *248*, 012059.

(3) Ou, Q.-F.; Xiong, B.-S.; Yu, L.; Wen, J.; Wang, L.; Tong, Y. In-Memory Logic Operations and Neuromorphic Computing in Non-Volatile Random Access Memory. *Materials* **2020**, *13*, 3532.

(4) Kim, D.; Jeon, Y. R.; Ku, B.; Chung, C.; Kim, T. H.; Yang, S.; Won, U.; Jeong, T.; Choi, C. Analog Synaptic Transistor with Al-Doped HfO_2 Ferroelectric Thin Film. *ACS Appl. Mater. Interfaces* **2021**, *13*, 52743−52753.

(5) Li, Y.; Fuller, E. J.; Sugar, J. D.; Yoo, S.; Ashby, D. S.; Bennett, C. H.; Horton, R. D.; Bartsch, M. S.; Marinella, M. J.; Lu, W. D.; Talin, A. A. Filament-Free Bulk Resistive Memory Enables Deterministic Analogue Switching. *Adv. Mater.* **2020**, *32*, 2003984.

(6) Ielmini, D.; Ambrogio, S. Emerging Neuromorphic Devices. *Nanotechnology* **2020**, *31*, 092001.

(7) Li, X.; Yu, B.; Wang, B.; Bao, L.; Zhang, B.; Li, H.; Yu, Z.; Zhang, T.; Yang, Y.; Huang, R.; Wu, Y.; Li, M. Multi-Terminal Ionic-Gated Low-Power Silicon Nanowire Synaptic Transistors with Dendritic Functions for Neuromorphic Systems. *Nanoscale* **2020**, *12*, 16348−16358.

(8) Feng, X.; Li, S.; Wong, S. L.; Tong, S.; Chen, L.; Zhang, P.; Wang, L.; Fong, X.; Chi, D.; Ang, K. W. Self-Selective Multi-Terminal Memtransistor Crossbar Array for In-Memory Computing. *ACS Nano* **2021**, *15*, 1764−1774.

(9) Lee, J.; Nikam, R. D.; Kwak, M.; Kwak, H.; Kim, S.; Hwang, H. Improvement of Synaptic Properties in Oxygen-Based Synaptic Transistors Due to the Accelerated Ion Migration in Sub-Stoichiometric Channels. *Adv. Electron. Mater.* **2021**, *7*, 2100219.

(10) Boyn, S.; Grollier, J.; Lecerf, G.; Xu, B.; Locatelli, N.; Fusil, S.; Girod, S.; Carrétéro, C.; Garcia, K.; Xavier, S.; Tomas, J.; Bellaiche, L.; Bibes, M.; Barthélémy, A.; Saïghi, S.; Garcia, V. Learning through Ferroelectric Domain Dynamics in Solid-State Synapses. *Nat. Commun.* **2017**, *8*, 14736.

(11) Luo, Z.; Wang, Z.; Guan, Z.; Ma, C.; Zhao, L.; Liu, C.; Sun, H.; Wang, H.; Lin, Y.; Jin, X.; Yin, Y.; Li, X. High-Precision and Linear Weight Updates by Subnanosecond Pulses in Ferroelectric Tunnel Junction for Neuro-Inspired Computing. *Nat. Commun.* **2022**, *13*, 699.

(12) Burr, G. W.; Shelby, R. M.; Sebastian, A.; Kim, S.; Kim, S.; Sidler, S.; Virwani, K.; Ishii, M.; Narayanan, P.; Fumarola, A.; Sanches, L. L.; Boybat, I.; Le Gallo, M.; Moon, K.; Woo, J.; Hwang, H.; Leblebici, Y. Neuromorphic Computing Using Non-Volatile Memory. *Adv. Phys.: X* **2017**, *2*, 89−124.

(13) Woo, J.; Moon, K.; Song, J.; Lee, S.; Kwak, M.; Park, J.; Hwang, H. Improved Synaptic Behavior under Identical Pulses Using AlO_x/HfO_2 Bilayer RRAM Array for Neuromorphic Systems. *IEEE Electron Device Lett.* **2016**, *37*, 994−997.

(14) Han, H.; Yu, H.; Wei, H.; Gong, J.; Xu, W. Recent Progress in Three-Terminal Artificial Synapses: From Device to System. *Small* **2019**, *15*, 1900695.

(15) Yu, S. Resistive Random Access Memory (RRAM). *Synth. Lect. Hum. Lang. Technol.* **2016**, *2*, 1−79.

(16) Guan, X.; Lei, Z.; Yu, X.; Lin, C. H.; Huang, J. K.; Huang, C. Y.; Hu, L.; Li, F.; Vinu, A.; Yi, J.; Wu, T. Low-Dimensional Metal-Halide Perovskites as High-Performance Materials for Memory Applications. *Small* **2022**, *18*, 2203311.

(17) Cao, Q.; Lü, W.; Wang, X. R.; Guan, X.; Wang, L.; Yan, S.; Wu, T.; Wang, X. Nonvolatile Multistates Memories for High-Density Data Storage. *ACS Appl. Mater. Interfaces* **2020**, *12*, 42449−42471.

(18) Balakrishna Pillai, P.; De Souza, M. M. Nanoionics-Based Three-Terminal Synaptic Device Using Zinc Oxide. *ACS Appl. Mater. Interfaces* **2017**, *9*, 1609−1618.

(19) Ielmini, D.; Pedretti, G. Device and Circuit Architectures for In-Memory Computing. *Adv. Intell. Syst.* **2020**, *2*, 2000040.

(20) Yu, S. Neuro-Inspired Computing with Emerging Nonvolatile Memorys. *Proceedings of the IEEE*, 2018; Vol. *106*, pp 260−285, 10.1109/jproc.2018.2790840.

(21) Go, J.; Kim, Y.; Kwak, M.; Song, J.; Chekol, S. A.; Kwon, J. D.; Hwang, H. W/WO_{3-x} Based Three-Terminal Synapse Device with Linear Conductance Change and High on/off Ratio for Neuromorphic Application. *Appl. Phys. Express* **2019**, *12*, 026503.

(22) Nikam, R. D.; Kwak, M.; Lee, J.; Rajput, K. G.; Hwang, H. Controlled Ionic Tunneling in Lithium Nanoionic Synaptic Transistor through Atomically Thin Graphene Layer for Neuromorphic Computing. *Adv. Electron. Mater.* **2020**, *6*, 1901100.

(23) Onen, M.; Emond, N.; Li, J.; Yildiz, B.; Del Alamo, J. A. CMOS-Compatible Protonic Programmable Resistor Based on Phosphosilicate Glass Electrolyte for Analog Deep Learning. *Nano Lett.* **2021**, *21*, 6111−6116.

(24) Lee, C.; Choi, W.; Kwak, M.; Kim, S.; Hwang, H. Impact of Electrolyte Density on Synaptic Characteristics of Oxygen-Based Ionic Synaptic Transistor. *Appl. Phys. Lett.* **2021**, *119*, 103503.

(25) Bisri, S. Z.; Shimizu, S.; Nakano, M.; Iwasa, Y. Endeavor of Iontronics: From Fundamentals to Applications of Ion-Controlled Electronics. *Adv. Mater.* **2017**, *29*, 1607054.

(26) Yao, X.; Klyukin, K.; Lu, W.; Onen, M.; Ryu, S.; Kim, D.; Emond, N.; Waluyo, I.; Hunt, A.; del Alamo, J. A.; Li, J.; Yildiz, B.; Yildiz, B. Protonic Solid-State Electrochemical Synapse for Physical Neural Networks. *Nat. Commun.* **2020**, *11*, 3134.

(27) Nikam, R. D.; Kwak, M.; Hwang, H. All-Solid-State Oxygen Ion Electrochemical Random-Access Memory for Neuromorphic Computing. *Adv. Electron. Mater.* **2021**, *7*, 2100142.

(28) Woo, J.; Yu, S. Impact of Selector Devices in Analog RRAM-Based Crossbar Arrays for Inference and Training of Neuromorphic System. *IEEE Trans. Very Large Scale Integr. Syst.* **2019**, *27*, 2205−2212.

(29) Valov, I.; Tsuruoka, T. Effects of Moisture and Redox Reactions in VCM and ECM Resistive Switching Memories. *J. Phys. D: Appl. Phys.* **2018**, *51*, 413001.

(30) Park, J.; Oh, C.; Son, J. Anisotropic Ionic Transport-Controlled Synaptic Weight Update by Protonation in a VO_2 transistor. *J. Mater. Chem. C* **2021**, *9*, 2521−2529.

(31) Pae, S.; Prasad, C.; Ramey, S.; Thomas, J.; Rahman, A.; Lu, R.; Hicks, J.; Batzer, S.; Zhao, Q.; Hatfield, J.; Liu, M.; Parker, C.; Woolery, B. Gate Dielectric TDDB Characterizations of Advanced High-k and Metal-Gate CMOS Logic Transistor Technology. *IEEE International Reliability Physics Symposium*, 2012; Vol. *5*, pp 1−5.

(32) Kim, S.; Ott, J. A.; Ando, T.; Miyazoe, H.; Narayanan, V.; Rozen, J.; Todorov, T.; Onen, M.; Gokmen, T.; Bishop, D.; Solomon, P.; Lee, K. T.; Copel, M.; Farmer, D. B. Metal-Oxide Based, CMOS-Compatible ECRAM for Deep Learning Accelerator. *IEEE International Electron Devices Meeting*, 2019; Vol. *35*, p 7.1.

(33) Yang, J. L.; Liu, L.; Yu, Z.; Chen, P.; Li, J.; Dananjaya, P. A.; Koh, E. K.; Lew, W. S.; Liu, K.; Yang, P.; Fan, H. J. Dielectric-Metallic Double-Gradient Composition Design for Stable Zn Metal Anodes. *ACS Energy Lett.* **2023**, *8*, 2042−2050.

(34) Prabhu, N. L.; Loy Jia Jun, D.; Dananjaya, P. A.; Lew, W. S.; Toh, E. H.; Raghavan, N. Exploring the Impact of Variability in Resistance Distributions of RRAM on the Prediction Accuracy of Deep Learning Neural Networks. *Electronics* **2020**, *9*, 414.

(35) Kumar, D.; Chand, U.; Siang, L. W.; Tseng, T. Y. ZrN-Based Flexible Resistive Switching Memory. *IEEE Electron Device Lett.* **2020**, *41*, 705−708.

(36) Huang, M.; Tan, A. J.; Mann, M.; Bauer, U.; Ouedraogo, R.; Beach, G. S. D. Three-Terminal Resistive Switch Based on Metal/Metal Oxide Redox Reactions. *Sci. Rep.* **2017**, *7*, 7452.

(37) Moon, K.; Cha, E.; Park, J.; Gi, S.; Chu, M.; Baek, K.; Lee, B.; Oh, S. H.; Hwang, H. Analog Synapse Device with 5-b MLC and Improved Data Retention for Neuromorphic System. *IEEE Electron Device Lett.* **2016**, *37*, 1067−1070.

(38) Messerschmitt, F.; Jansen, M.; Rupp, J. L. M. When Memristance Crosses the Path with Humidity Sensing—About the

https://doi.org/10.1021/acsami.3c03974
ACS Appl. Mater. Interfaces 2023, 15, 29287−29296

Importance of Protons and Its Opportunities in Valence Change Memristors. *Adv. Electron. Mater.* **2018**, *4*, 1800282.
(39) Messerschmitt, F.; Kubicek, M.; Rupp, J. L. M. How Does Moisture Affect the Physical Property of Memristance for Anionic-Electronic Resistive Switching Memories? *Adv. Funct. Mater.* **2015**, *25*, 5117−5125.
(40) Steinsvik, S.; Larring, Y.; Norby, T. Hydrogen Ion Conduction in Iron-Substituted Strontium Titanate, $SrTi_{1-x}Fe_xO_{3-x/2}$ ($0 \leq x \leq 0.8$). *Solid State Ionics* **2001**, *143*, 103−116.
(41) Oikawa, I.; Takamura, H. Correlation among Oxygen Vacancies, Protonic Defects, and the Acceptor Dopant in Sc-Doped $BaZrO_3$ Studied by 45Sc Nuclear Magnetic Resonance. *Chem. Mater.* **2015**, *27*, 6660−6667.
(42) Fabbri, E.; Bi, L.; Pergolesi, D.; Traversa, E. Towards the next Generation of Solid Oxide Fuel Cells Operating below 600 °C with Chemically Stable Proton-Conducting Electrolytes. *Adv. Mater.* **2012**, *24*, 195−208.
(43) Over, H.; Seitsonen, A. P. Oxidation of Metal Surfaces. *Science* **2002**, *297*, 2003−2005.
(44) Jana, D.; Maikap, S.; Prakash, A.; Chen, Y. Y.; Chiu, H. C.; Yang, J. R. Enhanced Resistive Switching Phenomena Using Low-Positive-Voltage Format and Self-Compliance LrO_x/GdO_x/W Cross-Point Memories. *Nanoscale Res. Lett.* **2014**, *9*, 12.
(45) Wu, G.; Wan, C.; Zhou, J.; Zhu, L.; Wan, Q. Low-Voltage Protonic/Electronic Hybrid Indium Zinc Oxide Synaptic Transistors on Paper Substrates. *Nanotechnology* **2014**, *25*, 094001.
(46) Tang, J.; Bishop, D.; Kim, S.; Copel, M.; Gokmen, T.; Todorov, T.; Shin, S.; Lee, K. T.; Solomon, P.; Chan, K.; Haensch, W.; Rozen, J. ECRAM as Scalable Synaptic Cell for High-Speed, Low-Power Neuromorphic Computing, 2018 *International Electron Devices Meeting*; Institute of Electrical and Electronics Engineers: San Francisco, 2018; pp 18:292−18:295.
(47) Nikam, R. D.; Lee, J.; Choi, W.; Banerjee, W.; Kwak, M.; Yadav, M.; Hwang, H. Ionic Sieving Through One-Atom-Thick 2D Material Enables Analog Nonvolatile Memory for Neuromorphic Computing. *Small* **2021**, *17*, 2103543.
(48) Islam, R.; Li, H.; Chen, P. Y.; Wan, W.; Chen, H. Y.; Gao, B.; Wu, H.; Yu, S.; Saraswat, K.; Philip Wong, H. S. Device and Materials Requirements for Neuromorphic Computing. *J. Phys. D: Appl. Phys.* **2019**, *52*, 113001.
(49) Lee, K.; Kwak, M.; Choi, W.; Lee, C.; Lee, J.; Noh, S.; Lee, J.; Lee, H.; Hwang, H. Improved Synaptic Functionalities of Li- Based Nano-Ionic Synaptic Transistor with Ultralow Conductance Enabled by Al_2O_3 Barrier Layer. *Nanotechnology* **2021**, *32*, 275201.
(50) Nielsen, M. A. *Neural Networks and Deep Learning*; Determination Press, 2015.

Recommended by ACS

Black Phosphorus/Ferroelectric P(VDF-TrFE) Field-Effect Transistors with High Mobility for Energy-Efficient Artificial Synapse in High-Accuracy Neuromorphic Comp...

Zhaoying Dang, Jianhua Hao, *et al.*
JUNE 07, 2023
NANO LETTERS
READ

Molecular Structure Engineering of Polyelectrolyte Bilayer-Based Memristors: Implications for Linear Potentiation and Depression Characteristics

Shaohui Kang, Jin Shi Zhao, *et al.*
FEBRUARY 27, 2023
ACS APPLIED NANO MATERIALS
READ

Molecular Dynamics Study on Swelling and Exfoliation Properties of Montmorillonite Nanosheets for Application as Proton Exchange Membranes

Yuhan Liu, Le Shi, *et al.*
JANUARY 27, 2023
ACS APPLIED NANO MATERIALS
READ

Ferroelectric Content-Addressable Memory Cells with IGZO Channel: Impact of Retention Degradation on the Multibit Operation

Masud Rana Sk, Bhaswar Chakrabarti, *et al.*
JANUARY 04, 2023
ACS APPLIED ELECTRONIC MATERIALS
READ

Get More Suggestions >

https://doi.org/10.1021/acsami.3c03974
ACS Appl. Mater. Interfaces 2023, 15, 29287−29296